

The Cosmic-Ray Energy Spectrum between 2 PeV and 2 EeV Observed with the TALE detector in monocular mode

R.U. Abbasi¹, M. Abe², T. Abu-Zayyad¹, M. Allen¹, R. Azuma³, E. Barcikowski¹, J.W. Belz¹, D.R. Bergman¹, S.A. Blake¹, R. Cady¹, B.G. Cheon⁴, J. Chiba⁵, M. Chikawa⁶, A. Di Matteo⁷, T. Fujii⁸, K. Fujita⁹, M. Fukushima^{8,10}, G. Furlich¹, T. Goto⁹, W. Hanlon¹, M. Hayashi¹¹, Y. Hayashi⁹, N. Hayashida¹², K. Hibino¹², K. Honda¹³, D. Ikeda⁸, N. Inoue², T. Ishii¹³, R. Ishimori³, H. Ito¹⁴, D. Ivanov¹, H.M. Jeong¹⁵, S.M. Jeong¹⁵, C.C.H. Jui¹, K. Kadota¹⁶, F. Kakimoto³, O. Kalashev¹⁷, K. Kasahara¹⁸, H. Kawai¹⁹, S. Kawakami⁹, S. Kawana², K. Kawata⁸, E. Kido⁸, H.B. Kim⁴, J.H. Kim¹, J.H. Kim²⁰, S. Kishigami⁹, S. Kitamura³, Y. Kitamura³, V. Kuzmin^{17*}, M. Kuznetsov¹⁷, Y.J. Kwon²¹, K.H. Lee¹⁵, B. Lubsandorzhev¹⁷, J.P. Lundquist¹, K. Machida¹³, K. Martens¹⁰, T. Matsuyama⁹, J.N. Matthews¹, R. Mayta⁹, M. Minamino⁹, K. Mukai¹³, I. Myers¹, K. Nagasawa², S. Nagataki¹⁴, R. Nakamura²², T. Nakamura²³, T. Nonaka⁸, A. Nozato⁶, H. Oda⁹, S. Ogio⁹, J. Ogura³, M. Ohnishi⁸, H. Ohoka⁸, T. Okuda²⁴, Y. Omura⁹, M. Ono¹⁴, R. Onogi⁹, A. Oshima⁹, S. Ozawa¹⁸, I.H. Park¹⁵, M.S. Pshirkov^{17,25}, D.C. Rodriguez¹, G. Rubtsov¹⁷, D. Ryu²⁰, H. Sagawa⁸, R. Sahara⁹, K. Saito⁸, Y. Saito²², N. Sakaki⁸, N. Sakurai⁹, L.M. Scott²⁶, T. Seki²², K. Sekino⁸, P.D. Shah¹, F. Shibata¹³, T. Shibata⁸, H. Shimodaira⁸, B.K. Shin⁹, H.S. Shin⁸, J.D. Smith¹, P. Sokolsky¹, B.T. Stokes¹, S.R. Stratton^{1,26}, T.A. Stroman¹, T. Suzawa², Y. Takagi⁹, Y. Takahashi⁹, M. Takamura⁵, M. Takeda⁸, R. Takeishi¹⁵, A. Taketa²⁷, M. Takita⁸, Y. Tameda²⁸, H. Tanaka⁹, K. Tanaka²⁹, M. Tanaka³⁰, S.B. Thomas¹, G.B. Thomson¹, P. Tinyakov^{7,17}, I. Tkachev¹⁷, H. Tokuno³, T. Tomida²², S. Troitsky¹⁷, Y. Tsunesada⁹, K. Tsutsumi³, Y. Uchihori³¹, S. Udo¹², F. Urban³², T. Wong¹, M. Yamamoto²², R. Yamane⁹, H. Yamaoka³⁰, K. Yamazaki¹², J. Yang³³, K. Yashiro⁵, Y. Yoneda⁹, S. Yoshida¹⁹, H. Yoshii³⁴, Y. Zhezher¹⁷, and Z. Zundel¹

¹ *High Energy Astrophysics Institute and Department of Physics and Astronomy, University of Utah, Salt Lake City, Utah, USA*

² *The Graduate School of Science and Engineering, Saitama University, Saitama, Saitama, Japan*

³ *Graduate School of Science and Engineering, Tokyo Institute of Technology, Meguro, Tokyo, Japan*

⁴ *Department of Physics and The Research Institute of Natural Science, Hanyang University, Seongdong-gu, Seoul, Korea*

⁵ *Department of Physics, Tokyo University of Science, Noda, Chiba, Japan*

⁶ *Department of Physics, Kinki University, Higashi Osaka, Osaka, Japan*

⁷ *Service de Physique Thorique, Universit Libre de Bruxelles, Brussels, Belgium*

⁸ *Institute for Cosmic Ray Research, University of Tokyo, Kashiwa, Chiba, Japan*

⁹ *Graduate School of Science, Osaka City University, Osaka, Osaka, Japan*

¹⁰ *Kavli Institute for the Physics and Mathematics of the Universe (WPI), Todai Institutes for Advanced Study, University of Tokyo, Kashiwa, Chiba, Japan*

¹¹ *Information Engineering Graduate School of Science and Technology, Shinshu University, Nagano, Nagano, Japan*

¹² *Faculty of Engineering, Kanagawa University, Yokohama, Kanagawa, Japan*

¹³ *Interdisciplinary Graduate School of Medicine and Engineering, University of Yamanashi, Kofu, Yamanashi, Japan*

¹⁴ *Astrophysical Big Bang Laboratory, RIKEN, Wako, Saitama, Japan*

¹⁵ *Department of Physics, Sungkyunkwan University, Jang-an-gu, Suwon, Korea*

¹⁶ *Department of Physics, Tokyo City University, Setagaya-ku, Tokyo, Japan*

¹⁷ *Institute for Nuclear Research of the Russian Academy of Sciences, Moscow, Russia*

¹⁸ *Advanced Research Institute for Science and Engineering, Waseda University, Shinjuku-ku, Tokyo, Japan*

¹⁹ *Department of Physics, Chiba University, Chiba, Chiba, Japan*

²⁰ *Department of Physics, School of Natural Sciences, Ulsan National Institute of Science and Technology, UNIST-gil, Ulsan, Korea*

²¹ *Department of Physics, Yonsei University, Seodaemun-gu, Seoul, Korea*

²² *Academic Assembly School of Science and Technology Institute of Engineering, Shinshu University, Nagano, Nagano, Japan*

²³ *Faculty of Science, Kochi University, Kochi, Kochi, Japan*

²⁴ *Department of Physical Sciences, Ritsumeikan University, Kusatsu, Shiga, Japan*

²⁵ *Sternberg Astronomical Institute, Moscow M.V. Lomonosov State University, Moscow, Russia*

²⁶ *Department of Physics and Astronomy, Rutgers University - The State University of New Jersey, Piscataway, New Jersey, USA*

²⁷ *Earthquake Research Institute, University of Tokyo, Bunkyo-ku, Tokyo, Japan*

²⁸ *Department of Engineering Science, Faculty of Engineering, Osaka Electro-Communication University, Neyagawa-shi, Osaka, Japan*

*Corresponding author

E-mail: tareq@cosmic.utah.edu

²⁹ Graduate School of Information Sciences, Hiroshima City University, Hiroshima, Hiroshima, Japan

³⁰ Institute of Particle and Nuclear Studies, KEK, Tsukuba, Ibaraki, Japan

³¹ National Institute of Radiological Science, Chiba, Chiba, Japan

³² CEICO, Institute of Physics, Czech Academy of Sciences, Prague, Czech Republic

³³ Department of Physics and Institute for the Early Universe, Ewha Womans University, Seodaaemun-gu, Seoul, Korea

³⁴ Department of Physics, Ehime University, Matsuyama, Ehime, Japan

*

Abstract

We report on a measurement of the cosmic ray energy spectrum by the **Telescope Array Low-Energy Extension (TALE)** air fluorescence detector. The TALE air fluorescence detector is also sensitive to the Cherenkov light produced by shower particles. Low energy cosmic rays, in the PeV energy range, are detectable by TALE as “Cherenkov Events”. Using these events, we measure the energy spectrum from a low energy of ~ 2 PeV to an energy greater than 100 PeV. Above 100 PeV TALE can detect cosmic rays using air fluorescence. This allows for the extension of the measurement to energies greater than a few EeV. In this paper, we will describe the detector, explain the technique, and present results from a measurement of the spectrum using ~ 1000 hours of observation. The observed spectrum shows a clear steepening near $10^{17.1}$ eV, along with an ankle-like structure at $10^{16.2}$ eV. These features present important constraints on galactic cosmic rays origin and propagation models. The feature at $10^{17.1}$ eV may also mark the end of the galactic cosmic rays flux and the start of the transition to extra-galactic sources.

1. Introduction

The TALE detector was designed to look for structure in the energy spectrum and associated change in composition of cosmic rays below the ankle structure at $10^{18.6}$ eV. The ankle structure has been observed now by a number of experiments, though the interpretation of the structure is still a matter of open debate. A possible explanation, one that would be consistent with a changing composition, is that the ankle represents the transition from galactic flux (below the ankle) to that of cosmic rays of extragalactic origin [1]. An alternative interpretation for the ankle is that it is a “dip” in the cosmic rays flux caused by the pair-production interaction of extragalactic protons with the cosmic microwave background (CMB) photons [2, 3]. The latter scenario would be consistent with the predominately protonic, composition reported by HiRes [4] and Telescope Array (TA) [5], and one would then expect a galactic-extragalactic transition to occur at a lower energy. Yet another interpretation of the ankle as the maximum energy at the source of extragalactic protons ($E_{max} \sim 5Z \times 10^{18}$ eV) has been proposed in light of Auger data [6]. This scenario also requires that the galactic-extragalactic transition to occur at an energy below that of the ankle.

Indications of a knee-like structure in the 10^{17} decade have been seen in the spectra reported by several previous experiments “e.g.” [7, 8, 9, 10]. As shown in Figure 1, the energy scales of these detectors differed by about a factor of two, so the energy at which this spectral break occurs is quite uncertain. However, each data set shows a definite softening (break) in the power law spectral index, that we call the *second knee*. When the energy scales are adjusted in the right half of Figure 1, the four spectra can be made to align simultaneously in normalization (flux) and in the location of the break. Thus, while we know the break in the spectrum exists, its energy is uncertain, except that it occurs somewhere in the 10^{17} eV decade. No real progress on understanding this important feature can occur until one single experiment measures all three spectral features of the ultra-high energy (UHE) cosmic ray regime: the high energy suppression (GZK cut-off), the ankle, and the second-knee.

Using both Fluorescence and Cherenkov light, the TALE fluorescence detector (FD) is able to push the minimum energy of the spectrum measurement to well below 10^{16} eV. This gives plenty of lever-arm for

* Deceased

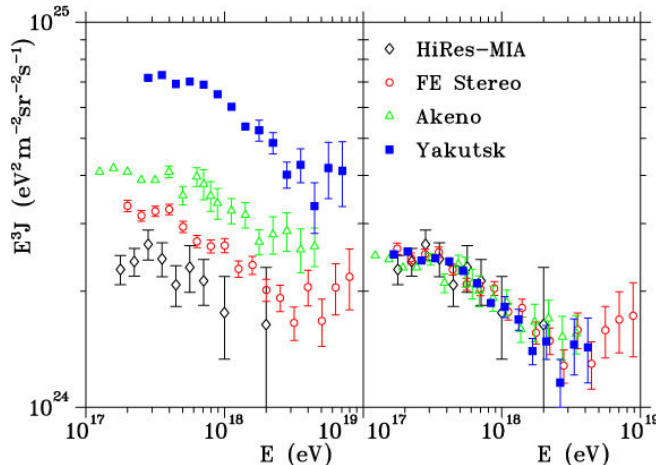


Figure 1: Left: Cosmic ray spectra measured by the Flys Eye [7], HiRes/MIA [8], Akeno [9], and Yakutsk [10] experiments. Each shows a flat part, a break, and a falling part (on an $E^3 J$ plot, where J denotes the differential flux). Right: Aligning the flat parts of the spectra from the four experiments, the spectral feature known as the second knee appears at the same energy, about $10^{17.5}$ eV. Below this energy the spectrum is flat (on an $E^3 J$ plot).

fitting the spectrum around the second knee feature to power laws, and also allow us to probe for additional spectral features down to the “first knee” near $10^{15.5}$ eV. At the same time, TALE measurements overlap that of the original TA detectors, and with a common energy scale. Hence TA/TALE will observe all three spectral features indicated above within the framework of a single experiment.

Further composition measurements below $10^{18.5}$ eV, from hybrid analysis (determining shower geometries using both TALE FD and TALE SD), will answer the question of the origin of the ankle and the second knee. With reliable and redundant measurements of the composition, one can also selectively analyze the heavy or light parts of the event sample to see where the second knee presents itself. Its presence in the heavy part of the data would indicate that the second knee is a galactic effect. Conversely, a second knee with light composition would suggest an extra-galactic origin for the effect.

This paper represents the first step in the TALE program, where we measure and present the cosmic ray spectrum from $10^{15.3}$ eV to $10^{18.3}$ eV. Only the high elevation (31° - 55°) telescopes of TALE FD, see section 2, are used, as the majority of interesting events in this range, especially toward the region of the second knee and below, register only in the upper elevation detector.

In the remainder of the paper, we will describe the detector and data collection in section 2, and explain the event selection procedure and event reconstruction method in section 3. Section 3 concludes with an overview of the spectrum measurement procedure. In section 4 we will describe the Monte Carlo (MC) simulation, and show its result for the detector aperture calculation. We will also present the results of MC studies of the reconstruction performance, in order to understand the detector resolution and validate the reconstruction technique. Finally, key distributions related to the aperture of the detector from the simulation will be compared to those from actual data in order to verify the accuracy of the detector simulation and the aperture calculation. Following a discussion of the systematic uncertainties in section 5, the measured spectrum will be shown in section 6, along with a brief discussion of the measured results. The paper will conclude with a summary in section 7.

2. TALE Detector and Operation

TA is an international collaboration with members from Japan, U.S., South Korea, Russia, and Belgium. The TA experiment is located in the West Desert of Utah, about 150 miles southwest of Salt Lake City, and is the largest cosmic ray detector in the northern hemisphere. In operation since 2008, TA consists of 507 surface detectors (SD), arranged in a square grid of 1.20 km spacing [11]. A total of 38 telescopes are distributed among three FD stations at the periphery of the SD array [12, 13]. The FD telescopes observe the airspace above the SD array. This arrangement of detectors is shown in Figure 2. TA is the direct successor to both the Akeno Giant Air Shower Array (AGASA) and High resolution Flys Eye (HiRes) experiments

[14, 15], incorporating the scintillation counter design of the former for the SD, and the fluorescence detector technique of the latter. The goal of TA is to clarify the origin of ultra-high energy cosmic rays (UHECR) and related extremely high energy phenomena in the universe. The results of measuring the energy spectrum, composition, and anisotropy in the arrival direction distribution for energies above $10^{18.2}$ eV have been published [16, 5, 17]

At the northern FD station (Middle Drum), a TA low-energy extension (TALE) detector [18] has been under construction since 2011. Ten new telescopes were added to the 14 of the TA FD at the site. All 24 were refurbished from components previously used by HiRes, and updated with new communications hardware. Whereas the original 14 TA FD telescopes, distributed in two rings, view between 3° to 31° in elevation, the new TALE FD telescopes cover between 31° to 59° . Both the TA and TALE telescopes view approximately southeast, over the part of the sky above the SD array. This arrangement is illustrated in Figure 3. The new telescopes of the TALE FD were completed in 2013, and have been taking data since the fall of that year.

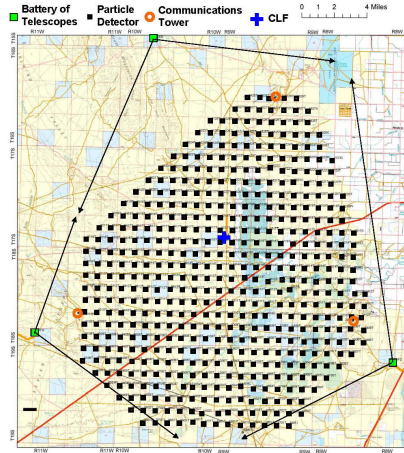


Figure 2: Map of the Telescope Array surface detector and the three fluorescence detectors overlooking the array. The MD site is at the green square at the top of the map.

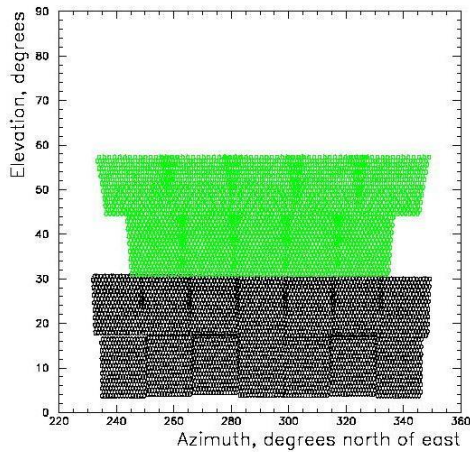


Figure 3: Schematic of TALE/MD mirrors showing azimuthal and elevation coverage. The aperture of the TA FD is shown in black, and TALE is shown in green.

In addition to the ten new, high-elevation angle, FD telescopes, TALE also incorporates 103 new SD counters arranged in a graded spacing array. The arrangement of the new counters is shown in Figure 4. As of the summer of 2017, all TALE SD counters are in place, and 80 are operational.

The TALE FD telescopes were assembled from refurbished HiRes-II mirrors, cameras, and readout electronics [19]. The mirrors are each made from four spherical segments arranged in a clover-leaf pattern. The

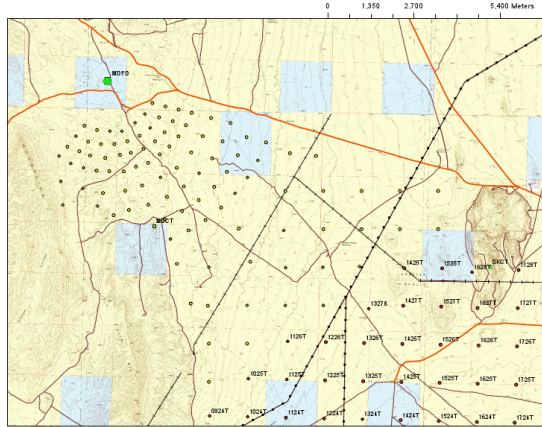


Figure 4: Map of the TALE surface detector. The TALE FD site can be seen near the top left of the figure

unobscured viewing area of each mirror is approximately 3.7 m^2 . A camera of 256 pixels is placed at the focal plane of the mirror. The pixels consist of 2-inch hexagonal XP3062 photo-multiplier tubes (PMTs) made by Photonis. They are arranged in a 16×16 hexagonal close-packed arrangement. Each pixel covers a one degree cone in the sky, and each camera has a field-of-view (FOV) of 16° in azimuth by 14° in elevation.

The PMT signals are recorded by a 10 MHz FADC readout system with an 8-bit resolution. Analog sums over rows and columns of pixels, also sampled at 8-bits, allow recovery of saturated PMTs in most cases. The summed signals are also used as the input to the trigger logic of the system, which looks for a three-fold coincidence in rows or in columns. The communications and timing systems were upgraded for TALE to include a LINUX-based link module that transfers telescope data to a central data acquisition (DAQ) computer over standard 100 Mbps Ethernet [20]. Inter-mirror triggers, GPS timing, and clock signals are distributed over a new custom serial system tied to a central timing module [21]. All of these replaced a token-ring like, proprietary fiber system of hires, and improved the data throughput from about 10 Mbytes/s to 100 Mbytes/s.

TALE FD construction began in 2011. The first observation runs with all 10 telescopes began in the September of that year. Over the following year, we continued to tune the gain and trigger of the system to achieve maximum data sensitivity while maintaining detector stability. These changes resulted in a number of distinct epochs of data that differ primarily in the separate settings of gain of the individual PMTs and those of the trigger analog row and column sums. Also, a set of filters, named “Moments and Clusters”, originally designed to remove Cherenkov-dominated blasts, were disabled at the beginning of 2015. In these events the detector sees an elliptical pattern left by the Cherenkov cone of an event coming toward the telescopes at small incident angles. During HiRes operation, such events were not written out. The removal of these filters was motivated in part by an attempt to run TALE FD in coincidence with a prototype non-imaging Cherenkov detector (NICHE) [22], and this change also improved TALE FD acceptance at energies below a few PeV. Table 1 summarizes the changes.

Table 1: TALE operation Epochs. Note that Moments/Clusters refer to high level online trigger routines which keep or reject telescope triggers based on tube trigger pattern (main use is to reject Cherenkov blasts.)

Epoch	Start	End	PMT gain	Trigger Gain	Moments/Clusters	Nightly UVLED Calib.
1	09/2013	01/2014	0.63	1.0	Yes	No
2	06/2014	01/2015	1.0	0.63	Yes	Yes
3	01/2015	current	1.0	0.63	No	Yes

A measurement of the cosmic-ray energy spectrum using TALE epoch 1 data has already been reported [23]. This paper deals with data collected during epochs 2 and 3.

Useful events recorded by TALE appear as tracks for which the observed signal comprises a combination of direct Cherenkov light (CL) and fluorescence light (FL), with some possible contribution from scattered

CL. Contributions of light generated by these mechanisms are both proportional to the number of charged particles in the extensive air shower (EAS) at any point along its development. Thus CL signals can be analyzed in a manner analogous to that for FL to determine the energy of the cosmic ray, and to determine the depth of shower maximum (X_{max}) which is related to the mass of the primary particle.

There are some important differences between CL and FL measurements. First, FL is emitted isotropically from the shower particles. In contrast CL is strongly peaked in the forward direction of the shower axis, and falls off rapidly as the incident angle of the shower to the detector increases. CL also accumulates along the shower and increases in overall intensity as the shower develops. Both types of light also undergo scattering in the atmosphere, from both molecules and particulate aerosols.

Figure 5 shows one extreme case of an event observed by the TALE FD where the shower axis lies more or less at right angle to the line of sight to the detector. The observed signal fitted to shower simulation shows that most of the signal seen is scintillation light (FL) observed directly (i.e. not scattered FL). This event is somewhat unusual in that it spans 55° in angle, and spread over five telescopes. It also has a very long time duration of about $13\mu\text{s}$.

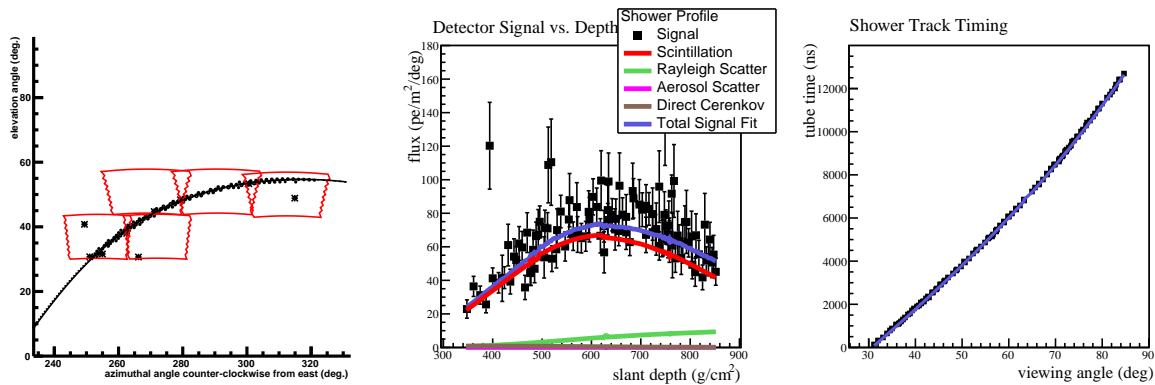


Figure 5: A five-telescope fluorescence event. The display panels show the event image (PMT trigger pattern), the reconstructed shower profile with relative contributions of FL/CL and scattered CL, and the time progression of triggered PMTs.

An illustration of an event of the opposite extreme is shown in Figure 6. This is a much lower energy event for which the shower axis points towards the detector at a small incident angle. Almost all of the signal registered comes from direct CL. As is typical of CL-dominated events, the event is short: it is contained in a single mirror, spanning just under 7° in angle, and only about 200ns in time.

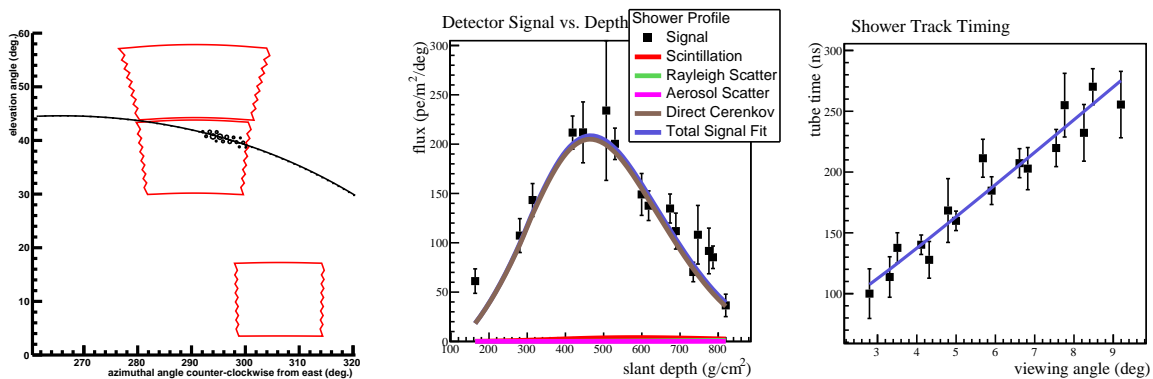


Figure 6: A one-telescope Cherenkov event. The display panels show the event image (PMT trigger pattern), the reconstructed shower profile with relative contributions of FL/CL and scattered CL, and the time progression of triggered PMTs.

The event set of TALE FD used in this paper contains a mix of CL and FL. However, at the lowest energies, events are dominated by CL. Because of the forward-beamed signal, those events pointing toward the detector are of course preferentially recorded. The cores of these showers fall within a small area near

the FD. At the higher energies, however, the FD becomes more sensitive to the isotropically emitted FL that can land over a much larger area around the detector site. In the decade between $10^{16.5}\text{eV}$ and $10^{17.5}\text{eV}$, the events are typically recorded with a mix of both CL and FL. The very different nature of the signals makes for somewhat complicated evolution of detector aperture and resolutions with energy, as will be discussed later in this paper.

3. Event Processing and Reconstruction

Nearly all of nightly data events from the TALE FD are from accidental coincident hits in PMTs from night-sky brightness fluctuations, and very low-energy Cherenkov blasts that cannot be used in the analysis. In order to reduce the data to contain only usable events, a processing chain was devised that analyzes the events and removes those which are of low quality. A brief description of the main steps and the data selection criteria used follows:

Step 1 Individual telescope data packets are combined to form “events”, and PMT signal calibration is applied.

Step 2 A shower-detector plane (SDP) is reconstructed from the pattern and pointing direction of the hit PMT pixels, as displayed in the left panels of figures 5 and 6. Directional correlation to the fitted SDP and expected time order are used to exclude accidental hits not related to the event. This procedure involves performing a *timing fit* of the hit pixels “time vs. angle”, as displayed in the right panels of figures 5 and 6. The following filtering criteria are then applied to select shower-induced, track-like events.

1. Arc length of track $> 4.5^\circ$
2. Inverse angular speed of track $> 0.012 \mu\text{s}/\text{deg}$
3. Event duration $> 0.1 \mu\text{s}$
4. Average number of photons/PMT > 50

The vast majority of the events removed at this stage actually failed the duration cut, mainly very low-energy Cherenkov blasts.

Step 3 Shower track reconstruction. The following selection criteria are applied to events at this stage:

1. Number of good-tubes (tubes associated with event) / deg of track > 1.1
2. timing fit normalized $\chi^2 < 5.0$

Step 4 Shower profile and energy reconstruction.

After the filtering cuts, the remaining events are subjected to full shower reconstruction, which includes the determination of shower geometry, energy, and the depth of shower maximum. In the original technique developed by the Flys Eye experiment [24], this process is divided into two steps. Shower geometry is determined by fitting the pattern of hit pixels to a shower detector plane (SDP), and then fitting the arrival time of light at the detector (in each hit pixel) as a function of the viewing angle of the pixel in the SDP:

$$t_i = t_0 + \frac{R_p}{c} \tan\left(\frac{\pi - \psi - \chi_i}{2}\right) \quad (1)$$

where R_p is the distance from the detector to the shower at the point of closest approach, ψ is the incline angle of the track in the SDP, t_0 is a time offset, and χ_i is the viewing angle of the i -th pixel.

Once the shower geometry is determined, the pixel directions are converted to shower depths, and the signal size is fitted to the light profile expected for a given energy and shower X_{max} according to the Gaisser-Hillas parameterization:

$$N(x) = N_{\text{max}} \times \left(\frac{x - X_0}{X_{\text{max}} - X_0}\right)^{(X_{\text{max}} - X_0)/\lambda} \exp\left(\frac{X_{\text{max}} - x}{\lambda}\right) \quad (2)$$

The parametrization gives the number of charged particles N at atmospheric depth x along the shower track. N_{\max} , X_{\max} , X_0 , λ are parameters. Here, N_{\max} is the number of shower particles at the point of maximum development, X_{\max} . X_0 represents the first point of interaction of the cosmic ray particle, and $\lambda = 70 \text{ g/cm}^2$, in combination with X_0 , sets the width of the shower profile curve.

The very low energy events observed by TALE, however, have track lengths that are too short for independent geometry reconstruction. So in this paper we use a simultaneous fit of the geometry and shower profile, but with holding the X_{\max} fit parameter fixed to some nominal value. This profile constrained geometry fit (PCGF) [25] was used successfully in the analysis of HiRes-I data, which made the first observation of the GZK suppression [26].

When applied to TALE events with significant CL signal, we found PCGF to give very good geometry resolutions. The sharply peaked CL in the forward direction constrains most of the light to within a few degrees from the true shower direction, which made the shower profile fit very sensitive to obtaining the correct pointing direction: After examining the results from multiple fits with different “trial” X_{\max} parameters we noticed that the reconstructed geometry was essentially independent from the assumed trial values. The resulting improvement of geometrical resolution (over that of monocular PCGF for FL dominated events) made it possible to measure the X_{\max} by adding a step to the reconstruction procedure in which the PCGF-determined geometry can be fixed and a shower profile fit following standard techniques can be performed.

The light signal recorded by a fluorescence detector contains a contribution from Cherenkov light generated by the shower particles. In event reconstruction, we distinguish among four contributions to the total observed light signal:

1. Direct Air Fluorescence light (FL).
2. Direct Cherenkov light (CL).
3. Rayleigh Scattered Cherenkov light
4. Aerosols Scattered Cherenkov light

These are the contributions to the total light signal shown in figures 5 and 6 by the different colors. All four contributions are included in the PCGF and in the MC simulation. The sum of the direct and scattered Cherenkov light make up the total CL signal.

The TALE FD monocular data set spans over three decades of energy. For optimizing the detector reconstruction algorithm and event selection at different energy ranges, we classified events into three categories:

1. Cherenkov event: Fractional contribution to total signal of CL > 0.75 and of direct CL > 0.55
2. Fluorescence events: Fractional contribution to total signal of FL > 0.75
3. Mixed events: those that do not belong to either (1) or (2) above.

As will be shown below, fluorescence events dominated at energies above $10^{17.5}$ eV, the Cherenkov events at below 10^{17} eV, and Mixed events in between. FL and CL events have very different characteristics. Mixed events may be more similar to CL or FL events depending on the direct CL contribution to the total signal. Different event selection criteria were chosen for the different types of events, as summarized in Table 2, in order to remove poorly reconstructed events and assure good detector resolution.

Table 2: Quality cuts applied to the three event categories. Note that some cut values are the same across the three subsets while others have different numerical values. Mixed events with direct CL fraction > 0.35 are subject to the same cuts as Cherenkov events.

Variable	CL	Mixed (dCL frac. < 0.35)	FL
Angular Track-length [deg]	$trk > 4.5^\circ$	$trk > 10.0^\circ$	$trk > 10.0^\circ$
Inverse angular speed [$\mu\text{s}/\text{deg}$]	$0.014 < 1/\omega < 0.1$	$0.06 < 1/\omega < 1.0$	$0.06 < 1/\omega < 1.0$
Shower Impact parameter [km]	$0.4 < R_p < 5.0$	$0.4 < R_p < 8.0$	$1.0 < R_p < 20.0$
Shower Zenith Angle [deg]	$28^\circ < \theta < 65^\circ$	$\theta < 65^\circ$	$\theta < 65^\circ$
Shower X_{\max} [g/cm^2]	$475 < X_{\max} < 815$	$525 < X_{\max} < 815$	$465 < X_{\max} < 815$
Estimated fit errors on energy		$\delta E/E < 0.6$	
Estimated fit errors on X_{\max} [g/cm^2]		$\delta X_{\max} < 200$	
Timing fit χ^2/dof		$\chi_{tim}^2 < 4.5$	
Profile fit χ^2/dof		$\chi_{pfl}^2 < 12$	

The same PCGF reconstruction code and event selection is applied to both data and simulated events. The performance of this technique will be discussed in a later section. Table 3 summarizes the number of events which survive the application of the quality cuts. The two time epochs comprising the total data set are listed separately as well.

Table 3: Number of TALE events and numbers in each category. The “After cuts” numbers include a requirement that the shower energy is greater than $10^{15.3}$ eV.

Data Set	Events	After Cuts
CL	883637	392758
Mixed	21102	3726
FL	8060	3578
All	912799	400062

The primary goal of the study described in this paper is to measure the energy spectrum of cosmic rays in the range $10^{15.3}$ to $10^{18.3}$ eV. Energy spectrum refers to the differential flux of cosmic rays, per unit energy, measured as a function of energy. We divide events in the data into bins of fixed width $\Delta x = \Delta \log_{10} E[\text{eV}] = 0.05$. For a given bin at energy E , the differential flux is then approximated by the formula:

$$J(E) = \frac{d^3N}{dEd(A\Omega)dt} \approx \frac{\Delta N}{\Delta E \Delta(A\Omega) \Delta t} \quad (3)$$

where ΔN is the number of events in the bin centered at energy E , $\Delta E = (\ln 10)E\Delta x$ is the width of the bin at energy E , $\Delta(A\Omega)$ is the aperture of the detector at energy E , and Δt the total run time. The product $\Delta(A\Omega)\Delta t$ is often referred to as the detector exposure.

Figure 7 shows the histogram of the energies of events in the data using the selection, reconstruction procedures, and quality cuts described in the preceding sections. These bin values then provide the numerator for equation 3. These data contains a total of 400,062 events with reconstructed energy greater than $10^{15.3}$ eV. These events were collected over a total observation time of 1080 hours, collected between June, 2014 and March, 2016. This observation time then provides one part of the denominator, Δt , of equation 3. ΔE is clearly defined by the binning. The only remaining quantity needed for evaluating the differential flux is the aperture.

As the symbol $(A\Omega)$ implies, the aperture is the product of the effective area and fiducial solid angle of the detector, which varies with energy. The effective area of the detector actually changes with the angular configuration of the events, so that $(A\Omega)$ actually represents a rather complicated convolution integral of the effective area multiplied by the solid angle element $d\Omega$ over all angular configurations. For this analysis, we evaluate $(A\Omega)$ using the Monte Carlo method, which we describe in the next section.

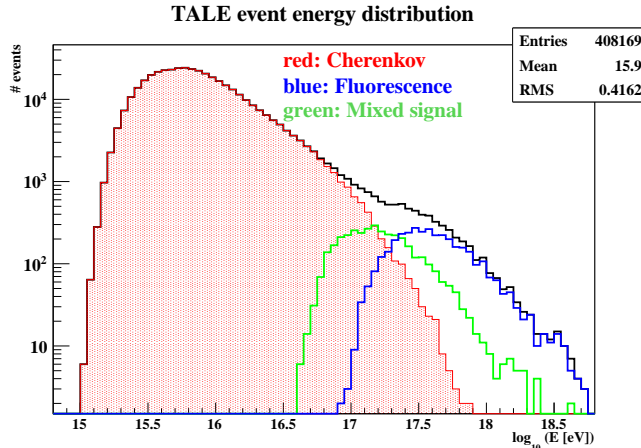


Figure 7: Histogram of the energies of events from TALE FD data. The distribution for Cherenkov, mixed, and fluorescence events are shown in red, green, and blue, respectively. The distribution for the inclusive set is shown in black. Note that the fluorescence events are restricted to energies above $\sim 10^{17}$ eV, the mixed events lowers the TALE FD threshold to about $10^{16.7}$ eV, and the Cherenkov events extends the reach by another 1.5 decades of energy to below $10^{15.5}$ eV. We should note that distributions obtained from the two data epochs look very similar to each other and to the combined histogram.

4. Simulation

The TALE simulation program is an updated version of the TA Middle Drum simulation program with added support for TALE. Much of the code is inherited from the HiRes-1 simulation program, with the exception of the TALE electronics simulation which has its origins in the HiRes-2 simulation package. The core of this code has been refined and tested against real data over a period of two decades. For TALE FD, the simulation uses actual run conditions: telescope live times, PMT gains, trigger settings, and atmospheric parameters, for each night of data collection.

The main components of the simulation are:

1. shower development and light production
2. light transmission through the atmosphere
3. detector optics ray-tracing
4. electronics signal processing
5. detector trigger logic

The longitudinal shower development is simulated using a library of showers created using the CONEX [27] package. MC events generated from this library are used to calculate the detector aperture. A smaller set of simulations generated from CORSIKA [28] is used to cross-check and validate the CONEX simulation. For instance, comparison between the two simulation sets are used to verify the missing energy correction.

A 4-parameter Gaisser-Hillas function is used to describe the longitudinal development of the shower. The lateral spread of the shower electrons is simulated according to a modified (NKG-like) parametrization from [30]. Simulation of fluorescence light production assumes the Kakimoto air fluorescence yield and the FLASH wavelength spectrum as in the case of previous TA papers [33, 34]. We also used a Cherenkov light angular distribution following the parametrization given in [35]. The amount of Cherenkov light production follows the Fly’s Eye formula [24] but with electron energy distributions updated to those given in [35].

Propagation of light from the shower to the detector are performed using photon-by-photon ray-tracing. The atmospheric profiles are provided from a GDAS database (one entry per three hour interval) [36]. Atmospheric aerosols density is treated as constant with an average density corresponding to a vertical aerosols optical depth (VAOD) of 0.04. Scattering and attenuation from Rayleigh, aerosol, and ozone scattering are all included.

The actual detector layout and geometry are reproduced in the MC. The shape and size of the telescope mirror, including obscurations from the PMT camera box, its mechanical supports, and cables are all included in the ray-tracing. Pixel response is modeled according to measured PMT cathode response profiles. Both

analog and digital readout electronics, including the trigger logic, are simulated in functional detail, with time development, including the effect of analog filters, and night-sky background light.

The simulation used for the detector aperture calculation is run as follows: A full energy range, 10^{15} - $10^{18.5}$ eV, set and a high energy, $10^{16.4}$ - $10^{18.5}$ eV, set were generated for the aperture calculation. The generated shower energies follow a $E^{-2.92}$ spectrum. The simulated showers are drawn from a shower library created using CONEX version 4.36 with QGSJet II-3 hadronic interaction model. Five primaries: H, He, N, Mg, and Fe are included in the simulations with a relative abundance based on the H4a model [37].

In addition to the above model, we fit the X_{\max} (data) distributions observed by the TALE FD to a mixture of four primaries (H, He, N, Fe), as a function of energy, and use the resulting abundances in our simulation. The fit is performed by calculating a weighted sum of four MC histograms representing the reconstructed X_{\max} distributions of the four primaries [38, 39]. A "thrown fraction" is then determined taking into account the relative detection and reconstruction efficiencies for each primary type. We refer to this primary mixture as "TXF", for TALE X_{\max} distributions Fits.

This process of fitting the observed X_{\max} distributions puts simulated showers in the actual positions in the sky as the real showers in the data, and is independent of hadronic interaction model. As will be seen below, our reconstruction of X_{\max} has excellent resolution below about $10^{17.5}$ eV, so the fitting process successfully simulates the data. Above this energy, although the resolution is not as good, the aperture is quite insensitive to composition, as will be shown in section 6, and so this process is robust. Figure 8 shows the aperture for this mix of primaries.

Simulated showers are reconstructed using the same procedure applied to real data, and event selection is done in the same way. A missing energy correction is applied to the reconstructed data and MC showers based on the same composition assumption, with the correction for each primary type and energy being estimated from the CONEX generated showers (cross checked against CORSIKA predictions). We use QGSJet II-3 because, at higher energies, we have measured[40] the missing energy using a technique invented by the Auger collaboration, and found that it agrees well with that predicted by QGSJet II-3.

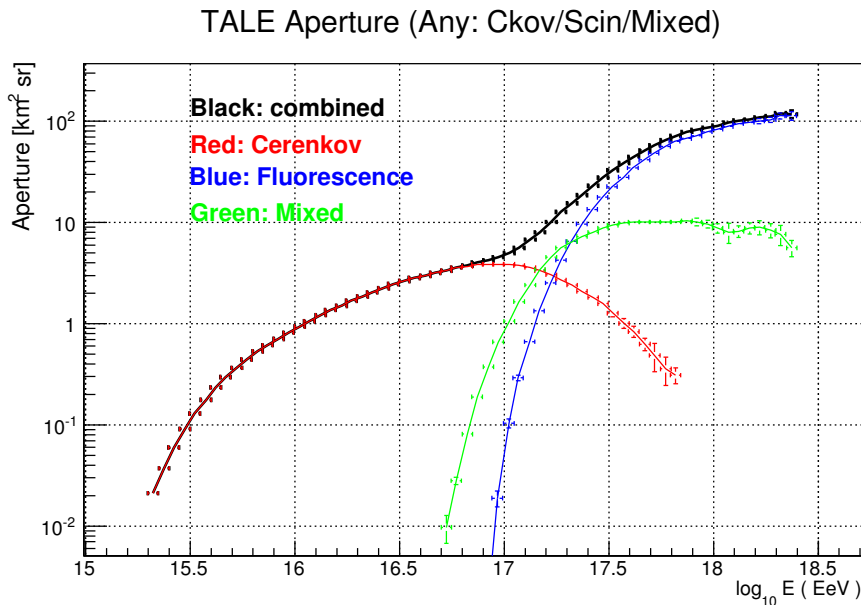


Figure 8: TALE aperture using the combined set of events. Aperture functions for each of the three subsets also shown.

In addition to calculating the aperture, the simulation is also used to verify the accuracy of the event reconstruction procedure. In particular we examine the reconstruction resolution of the following parameters:

1. The angle in the shower-detector plane, ψ
2. The shower impact parameter to the detector, R_p
3. The depth of shower maximum, X_{\max} .
4. The shower energy, E

Figures 9 - 12 show the difference between the reconstructed and thrown values of simulated events, for these four key variables. To understand how the reconstruction and quality cuts affect the different types of events, we show for each figure four resolution plots: Cherenkov (all energies), Cherenkov ($E > 10^{16.7}$ eV), Mixed signal, and fluorescence events separately.

For the fluorescence events in figures 9 - 12, we obtain resolutions of $\sim 5^\circ$ for $d\psi$, $\sim 5\%$ for dR_p/R_p , and ~ 60 g/cm² for dX_{\max} . These resolutions are comparable to those obtained for profile-constrained monocular reconstruction in previous studies [41]. However, the corresponding resolutions for mixed events and Cherenkov events ($E > 10^{16.7}$ eV) are much better than for fluorescence: $\sim 1^\circ$ for $d\psi$, 2-3% for dR_p/R_p , and ~ 35 g/cm² for dX_{\max} . The improvement is primarily due to the tight constraint in the reconstructed orientation of the shower from the strong forward peaking of direct Cherenkov light. For the whole Cherenkov set, which is dominated by those events below $10^{16.7}$ eV, we see that $d\psi$, dR_p/R_p and dX_{\max} increase to $\sim 1.6^\circ$, ~ 0.10 and ~ 45 g/cm², mostly as the result of shorter track lengths and event durations at the lowest energies. In all cases, the bias in the reconstruction are negligible compared to the resolutions.

Figure 12 shows the resolutions for the reconstructed energy. Here we see $\sim 16\%$ for dE/E in all Cherenkov events, and $\sim 9\%$ in Cherenkov events with $E > 10^{16.7}$ eV and in Mixed events. dE/E only increases slightly to about 10% for the case of fluorescence events. In the last case, we manage to obtain a good energy resolution in spite of relatively large $d\psi$ and dX_{\max} , as we had seen in previous application of the profile-constrained monocular fit [41]. The reason for this is that reconstruction errors in ψ and X_{\max} are highly correlated along a direction orthogonal to errors in the reconstructed R_p and energy. For the full range of the data set, we also see negligible bias in the reconstruction energy values. These results show that our reconstruction procedure is clearly adequate for the spectrum study presented in this paper.

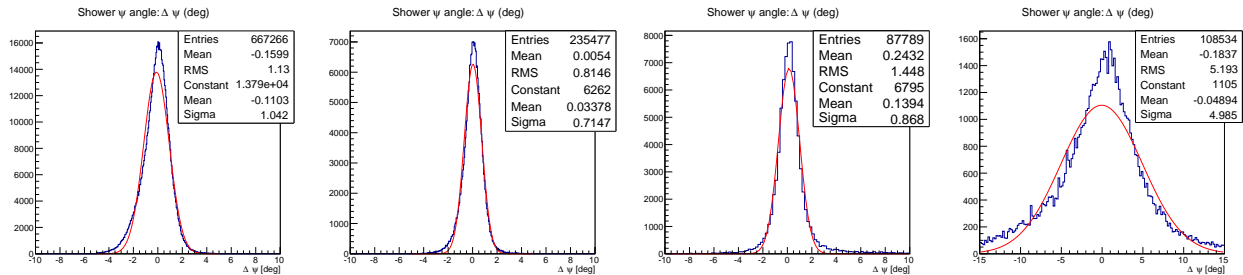


Figure 9: Shower angle in the plane ψ resolution after all quality cuts are applied. From the left: Cherenkov (all energies), Cherenkov ($E > 10^{16.7}$ eV), Mixed, and fluorescence events subsets. MC using a mixed composition, matching TXF results,

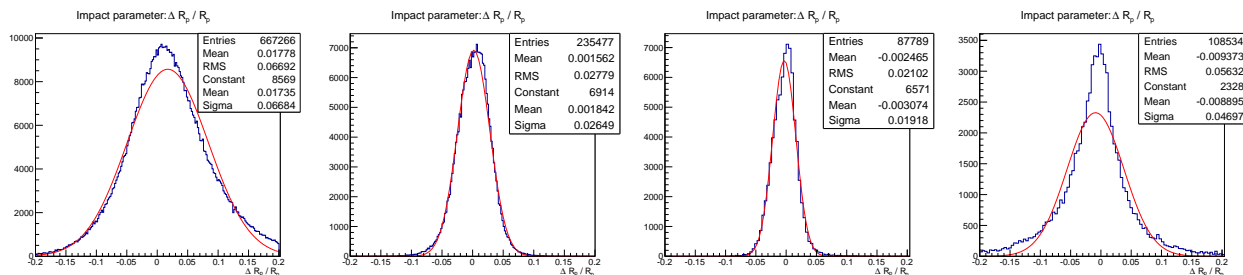


Figure 10: Shower impact parameter to the detector, R_p , resolution after all quality cuts are applied. From the left: Cherenkov (all energies), Cherenkov ($E > 10^{16.7}$ eV), Mixed, and fluorescence events subsets. MC using a mixed composition, matching TXF results,

The analysis depends on the MC simulation in two critical ways: (a) The event quality cuts were chosen according to their effect on the reconstruction resolution for simulated events, and (b) the aperture of the detector is calculated from the acceptance of the simulated events through the reconstruction and quality cuts. It is therefore important that the simulation gives an accurate account of the data. In Figure 13 and 14 we show the comparisons between distribution from the data to those of the MC for the event duration, and for the track length. The MC distribution in each case has been normalized to the number of data events, and

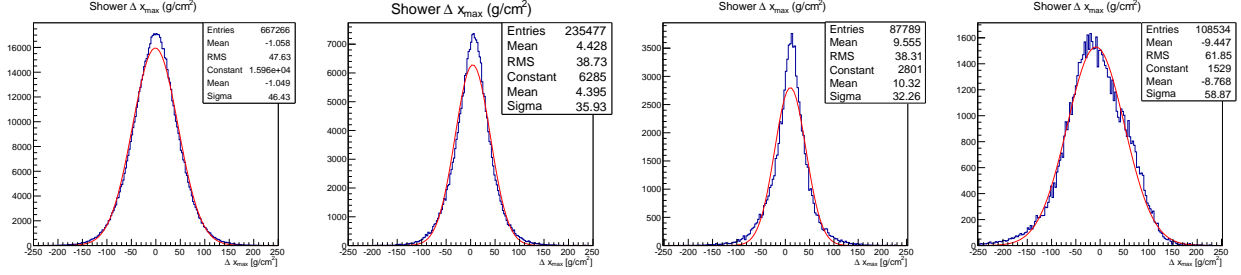


Figure 11: Shower X_{\max} resolution after all quality cuts are applied. From the left: Cherenkov (all energies), Cherenkov ($E > 10^{16.7}$ eV), Mixed, and fluorescence events subsets. MC using a mixed composition, matching TXF results,

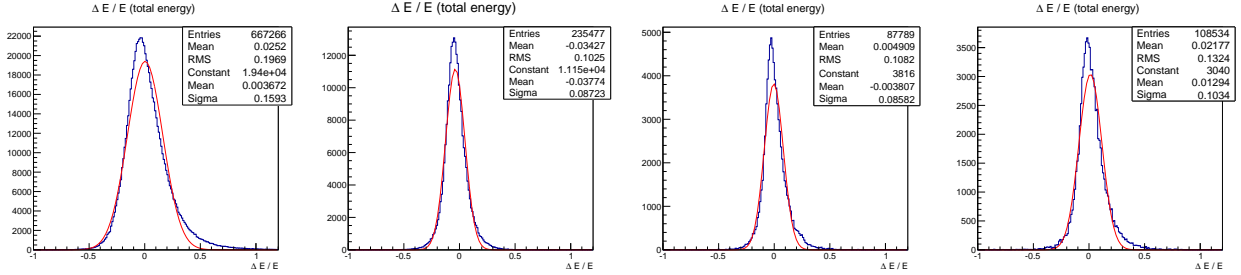


Figure 12: Shower energy resolution after all quality cuts are applied. From the left: Cherenkov (all energies), Cherenkov ($E > 10^{16.7}$ eV), Mixed, and fluorescence events subsets. MC using a mixed composition, matching TXF results,

the comparisons have been split between Cherenkov, Mixed, and fluorescence events. Two MC distributions are shown in each plot, one using the thrown MC distribution (H4a composition), and the other being the re-weighted distribution resulting from the TALE X_{\max} distributions fits (TXF). All of these plots show good agreement between data and MC.

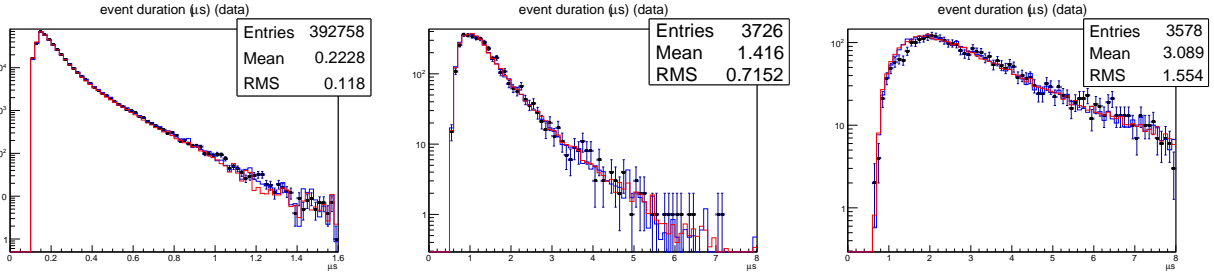


Figure 13: Total event duration (μs), for Cherenkov (left), Mixed (center), and fluorescence events (right). Black points are data, blue / red histograms are MC with mixed composition (H4a / TXF respectively).

The aperture calculation essentially measures the detection volume and angular acceptance of the detector and analysis procedures. The three most important parameters in this regard are (a) the impact parameter R_p , (b) the depth of shower maximum, X_{\max} , and (c) the zenith angle of the shower, θ . The distributions of R_p and X_{\max} approximately define the fiducial volume of the atmosphere for the fluorescence detector, and the zenith angle distribution gives the acceptance solid angle. For completeness we also include the azimuthal angle of the shower, ϕ . The data-MC comparisons for R_p , θ , and ϕ , separately for Cherenkov, Mixed, and fluorescence events, are given in figures 15 and 17. These distributions are again in good agreement between data and MC.

The X_{\max} distributions are shown in different energy ranges in figure 18. Here it should be noted that the TXF histograms are the results of fitting the X_{\max} distributions, and therefore “match” the data much better than the H4a composition model. The data used for the TXF only includes Cherenkov events and Mixed events, it does not include any fluorescence events.

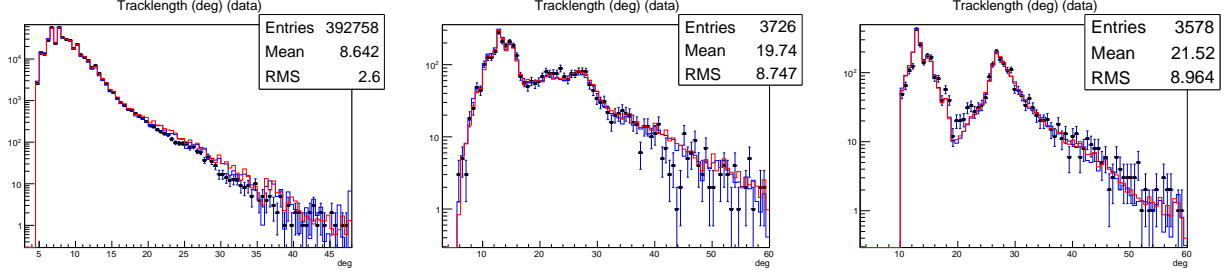


Figure 14: Angular track-length (deg), for Cherenkov (left), Mixed (center), and fluorescence events (right). Black points are data, blue / red histograms are MC with mixed composition (H4a / TXF respectively).

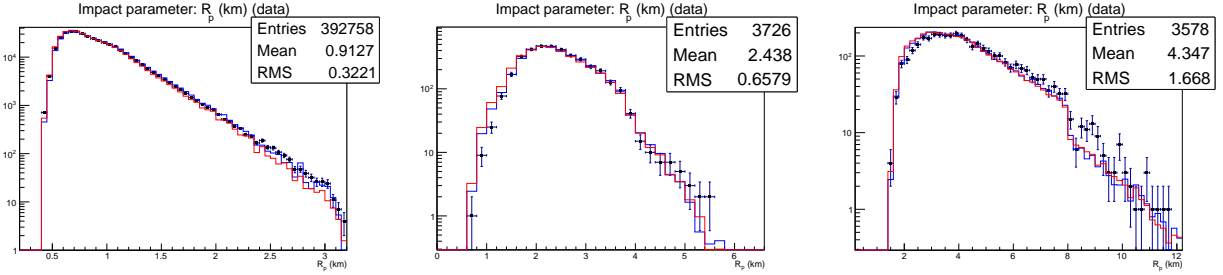


Figure 15: Shower impact parameter (km), for Cherenkov (left), Mixed (center), and fluorescence events (right). Black points are data, blue / red histograms are MC with mixed composition (H4a / TXF respectively).

Throughout this section we have presented the detector aperture, reconstruction resolution, and data/MC comparisons for a combined data set which includes epoch 2 and epoch 3 of TALE operation. This is justified by the fact that the only difference between the two epochs is the removal, in epoch 3, of the online Cherenkov “Blasts” filter. Even when allowed by the removal of the online filter, the vast majority of these events get filtered out by the offline analysis, starting with the filtering procedure described in “Step 2” of section 3, and also by later reconstruction steps and the application of quality cuts to the final reconstructed events set.

We examined data from the two epochs separately and found only minor differences at energies below $\sim 10^{15.5}$ eV. Since these blasts are mostly showers with energies of $\sim 10^{15}$ eV or less, we expect that the difference to be due to some of these events getting through. At energies above $\sim 10^{15.5}$ eV the distributions obtained from the different epochs and the expected reconstruction resolutions are similar.

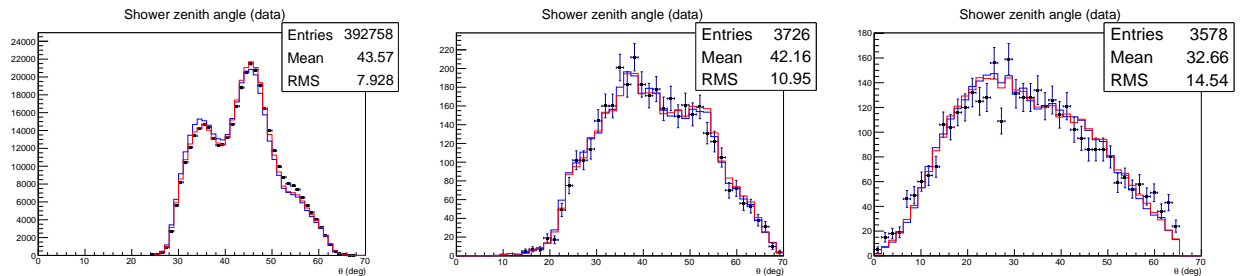


Figure 16: Shower zenith angle (deg), for Cherenkov (left), Mixed (center), and fluorescence events (right). Black points are data, blue / red histograms are MC with mixed composition (H4a / TXF respectively).

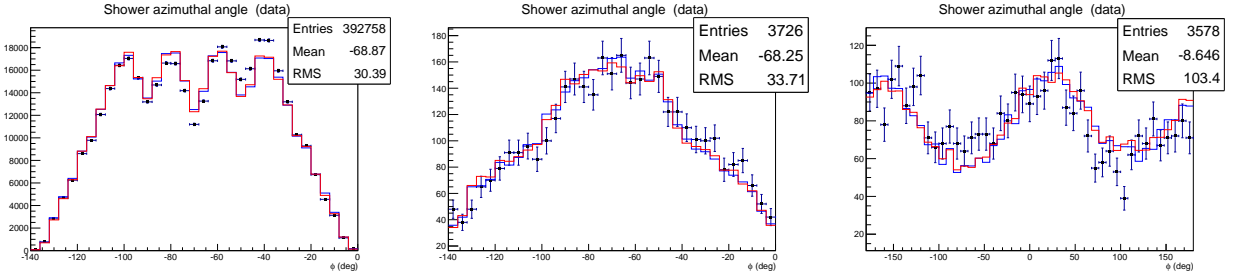


Figure 17: Shower zenith angle (deg), for Cherenkov (left), Mixed (center), and fluorescence events (right). Black points are data, blue / red histograms are MC with mixed composition (H4a / TXF respectively).

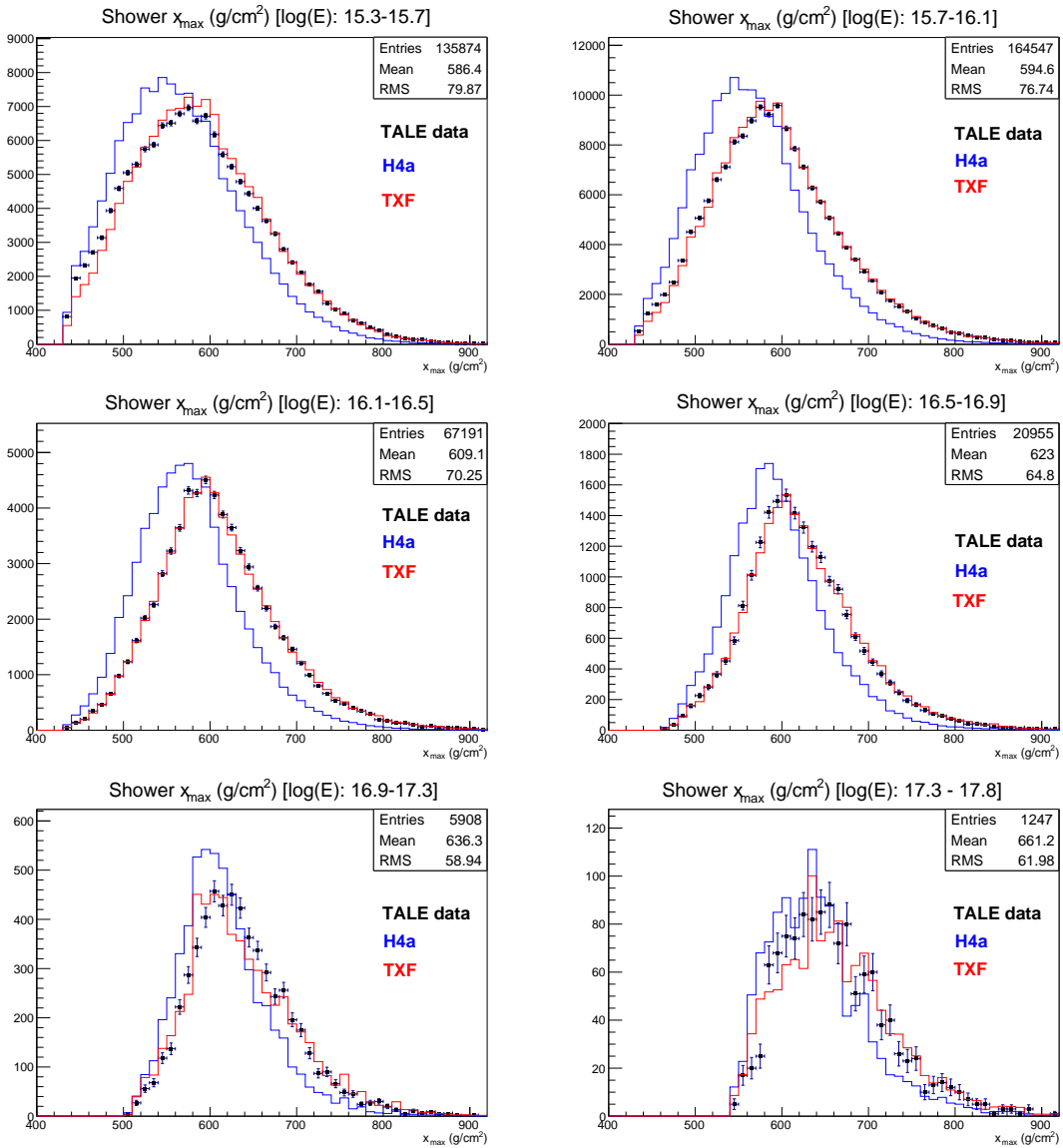


Figure 18: Shower X_{\max} (g/cm²), in different energy ranges. Black points are data, blue / red histograms are MC with mixed composition (H4a / TXF respectively). Note that the TXF histogram is a fit to the data.

5. Systematic Uncertainties

The main sources of systematic uncertainty in the measured flux come from the uncertainty in the energy scale which comes from a combination of uncertainties in the TALE fluorescence detector photonic scale, atmospheric corrections for scattering by aerosols of fluorescence and Cherenkov light, the fluorescence yield, and the correction for energy carried away (mostly) by neutrinos and muons that does not appear calorimetrically. The spectrum uncertainty consists of the energy scale uncertainty squared plus the uncertainty in the aperture, which mostly arises from the uncertainty in composition. A brief description of these sources follows:

Detector photonic scale This includes effects such as PMT gain, UV filter transmission, telescope mirror reflectivity, etc. The estimate is based on previous studies by the HiRes collaboration [42]. As already mentioned, the TALE FD uses refurbished HiRes-II telescopes.

Shower missing energy Estimate is based on two factors: (1) the dependence of the missing energy correction on the primary type, and (2) the dependence of the magnitude of the missing energy correction on the primary particle’s energy. The magnitude of the correction decreases with increasing energy, and the absolute separation between different primary types decreases as well, as can be seen in figure 19.

Atmosphere The attenuation of the shower signal by aerosols is modeled using an average aerosol density obtained from previous studies by the HiRes collaboration [42]. TALE is located at ~ 100 km south of the original HiRes detectors and shares similar climate and weather patterns. Aerosol measurements at the TA sites [43] also confirm the aerosol density is similar to that seen at HiRes. Nightly fluctuations about the average aerosol density have a small effect on the measured spectrum.

Fluorescence yield Several measurements of the absolute air fluorescence yield have been made, as summarized in the following references [44, 45]. Using an average yield based on multiple measurements leads to an estimate of the uncertainty of 6% on the energy due to the fluorescence yield, as described in [42] and used in [46]. Another approach is to combine the errors reported by the two experiments [33, 34], as was done in [55], and this leads to an energy uncertainty estimate of 11%. We use a value of 10%..

Composition The distribution of X_{max} values in the sky above the detector determines the distances of the brightest parts of the shower relative to the detector, and therefore affects how much light is collected by the telescope mirror. This has a direct impact on the detector aperture estimation.

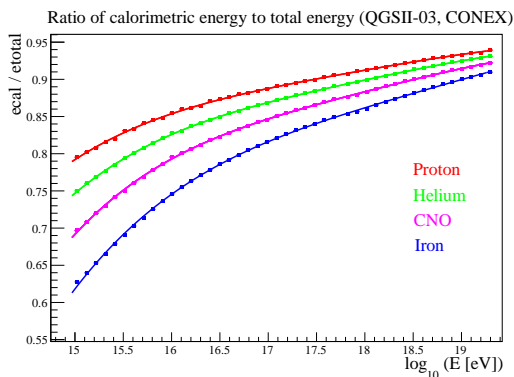


Figure 19: Ratio of calorimetric energy to total shower energy as given by CONEX simulations. Simulation sets of mono-energetic showers were used to calculate the ratio. Each point in the figure represents a simulation set and the curves represent a 4-th degree polynomial fit to the point

Table 4 shows the contributions from the various sources, and shows that the systematic uncertainty in the spectrum is approximately constant as a function of energy. Events with energy $E < 10^{17}$ eV occur so close to the detector that there is essentially no atmospheric effect. They are seen almost totally in Cherenkov light so are independent of the fluorescence yield. Events at 10^{18} eV occur within about 10 km

of the detector, and are also insensitive to atmospheric corrections. In both cases the composition-caused uncertainty in the aperture is minimal. For lower energy events we measure X_{\max} accurately and simulate the position of showers in the atmosphere in a model-independent way. For higher energy events we do the same, and in addition the aperture is insensitive to composition.

Table 4: Estimates of systematic uncertainties in the TALE FD energy scale and spectrum measurement. This uncertainty is approximately constant as a function of energy

Energy	Source	value	contribution to spectrum
$< 10^{17}$ eV	photonic scale	10%	20%
$< 10^{17}$ eV	missing energy	10%	20%
$< 10^{17}$ eV	atmosphere	0	0
$< 10^{17}$ eV	fluorescence yield	0	0
$< 10^{17}$ eV	composition (X_{max})	3%	6%
10^{18} eV	photonic scale	10%	20%
10^{18} eV	missing energy	5%	10%
10^{18} eV	atmosphere	2%	4%
10^{18} eV	fluorescence yield	10%	20%
10^{18} eV	composition (X_{max})	3%	6%
$< 10^{17}$ eV	total	14%	29%
10^{18} eV	total	15%	31%

6. Results and Discussion

The measured spectrum using data from June of 2014 through March 2016 is shown in figure 20. The systematic errors shown with the gray band in the figure are calculated by evaluating the effect on the spectrum of a systematic shift in the real data events energies of 15% either up or down, see table 4.

To calculate the systematic error band shown in the figure, reconstructed real data event energies were shifted up or down by 15%. A broken power-law fit, with two break points is also shown in the figure. The fit was performed in the range $10^{15.7} - 10^{18.3}$ eV, with the locations of the break points being free parameters. A summary of the fit results is shown in table 5.

The points in the spectrum shown in figure 20 are a combination of three separate subsets of events; each of which can be used to calculate an energy spectrum as shown in figure 21. A comparison of the spectra measured by using the three event categories in the energy range where they overlap shows that, within statistics, there is good agreement between Cherenkov dominated, fluorescence dominated, and mixed signal events.

Table 5: Fit parameters to a broken power law fit to TALE spectrum.

Break point 1: $\log_{10}(E)$	16.22 ± 0.017
Break point 2: $\log_{10}(E)$	17.04 ± 0.035
Spectral index: $15.70 < \log_{10}(E) < 16.22$	3.12 ± 0.007
Spectral index: $16.22 < \log_{10}(E) < 17.04$	2.92 ± 0.008
Spectral index: $17.04 < \log_{10}(E) < 18.30$	3.19 ± 0.017

While not part of the fit, it is easily seen from the spectrum plot that there is a significant spectral index change at around $\sim 10^{15.6}$ eV. A comparison of this energy and the second break point in table 5 shows that they are separated in energy by a factor of ~ 25 . This is somewhat suggestive in that if we interpret the low energy break as the “proton knee”, then the higher energy break occurs at where we would expect the “iron knee” to be according to the idea of rigidity dependent cutoffs in the spectra of individual nuclei as first proposed by Peters [47].

To examine the composition dependence of the spectrum, and to demonstrate the applicability of the aperture calculation using a primary mixture from the TXF to the high energy end of the spectrum, we

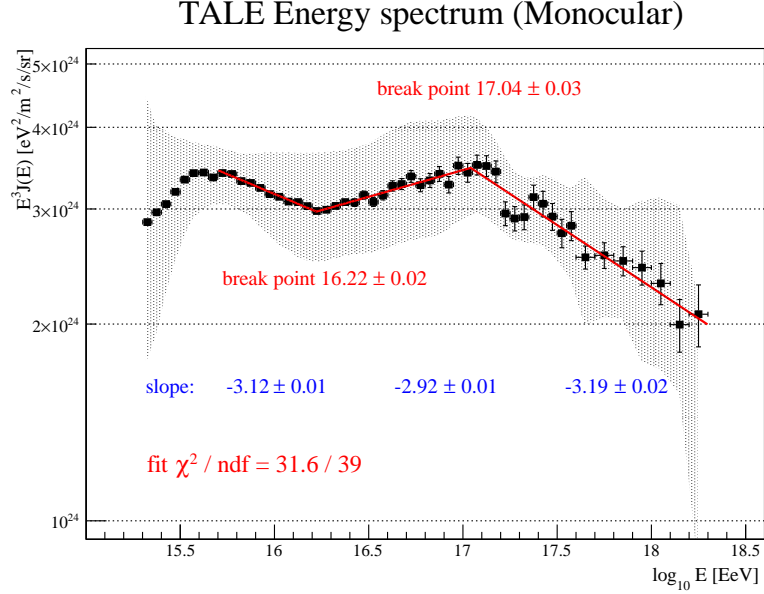


Figure 20: TALE cosmic rays energy spectrum measured with 22 months of data. A mixed primary composition given by the TXF is assumed. The gray band indicates the size of the systematic uncertainties.

show in figure 22 a comparison of the spectrum obtained with different compositions. With respect to the energy spectrum for the case of pure iron composition assumption, note that composition measurements by other experiments, e.g. [48, 49] exclude the possibility of iron dominated flux at energies below 10^{16} eV. The spectrum is included in the plot simply to demonstrate the extreme case of all heavy primaries.

Figure 23 compares the current result with some recent results from other experiments. We note that qualitatively the spectra are in agreement. The difference in normalization is within the systematics of the energy scale of the different experiments. In particular, we note that a 6.5% downward shift in the IceTop energy scale, results in a spectrum that lies on top of the TALE spectrum for energies below 10^{17} eV.

Figure 24 compares the current result with some recent results from TA Fluorescence [55] and surface detector [56] measurements. We note that above 10^{17} eV there is excellent agreement between the different results, demonstrating that the TALE spectrum can be seen as an extension of the measurements in the ultra-high energy regime down to lower energies.

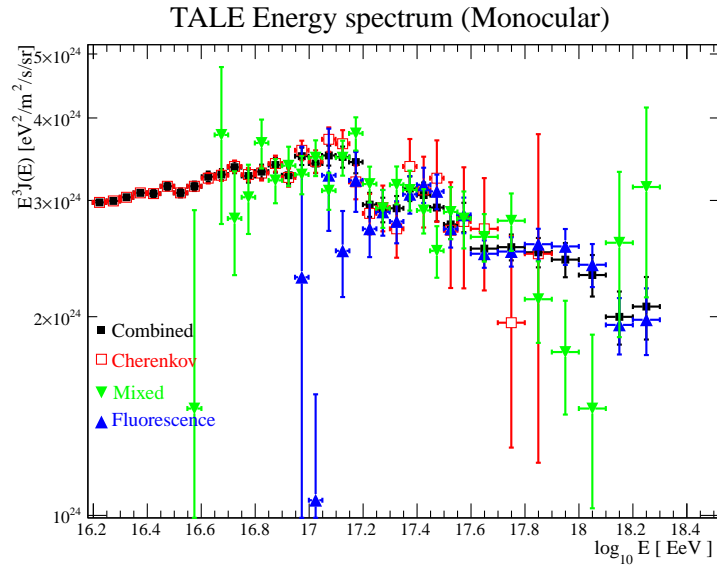


Figure 21: TALE cosmic rays energy spectrum measured with 22 months of data. Contributions from Cherenkov, mixed, and fluorescence events shown separately. Note that only the Cherenkov subsets contributes to the spectrum below $10^{16.7}$ eV.

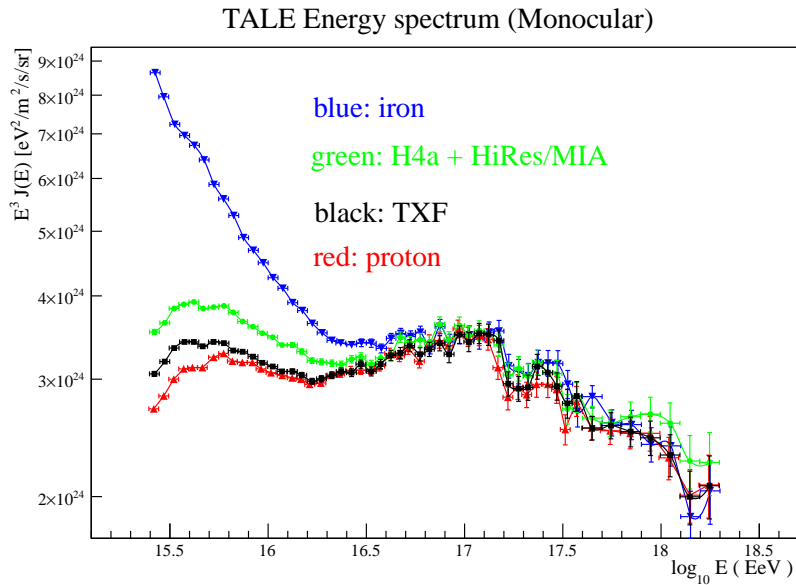


Figure 22: TALE cosmic rays energy spectrum composition dependence. A comparison of the spectrum calculation if we assume that cosmic rays are pure protons (red), pure iron (blue), follow the H4a composition (green), or the TXF result (black). The pure iron case is shown for reference only, at low energies it is excluded by previous measurements: e.g. [48, 49]

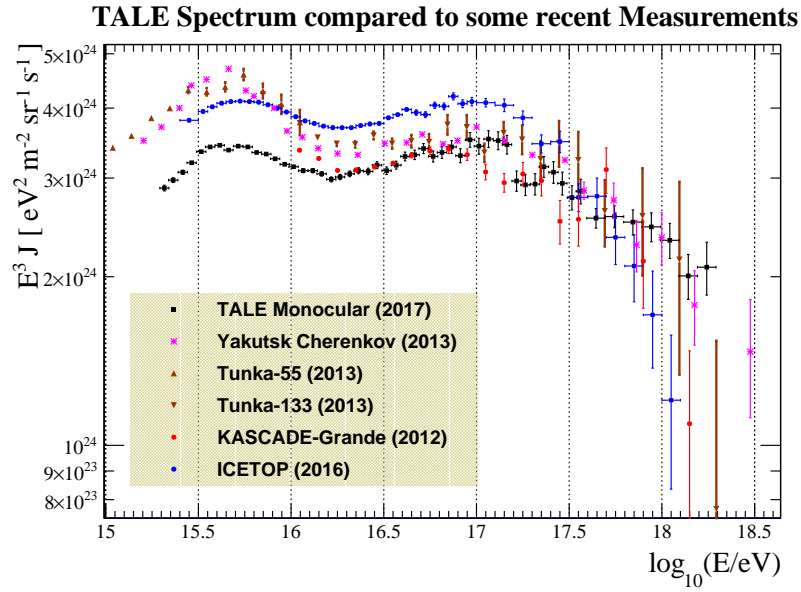


Figure 23: TALE cosmic rays energy spectrum plotted along with measurements by Yakutsk [50], TUNKA [51, 52], Kaskade-Grande [53], and IceTop [54]

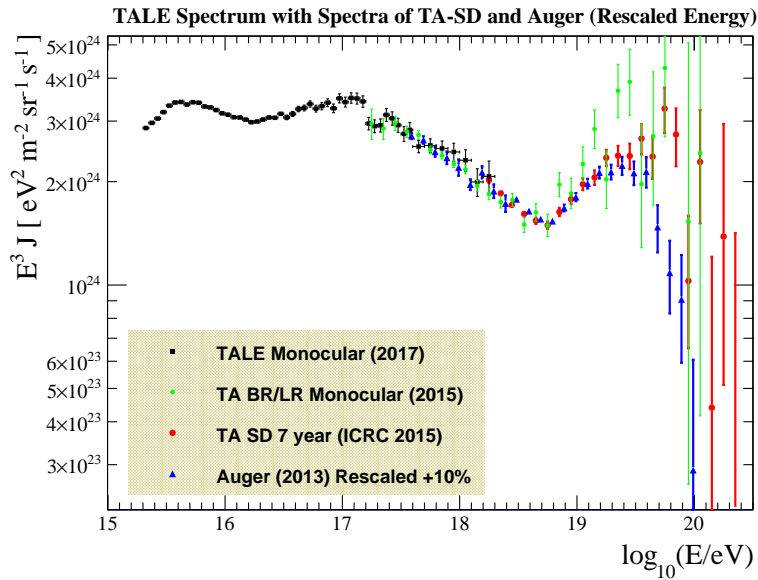


Figure 24: TALE cosmic rays energy spectrum plotted along with measurements by TA using the FD's at Black Rock and Long Ridge sites [55], and by the TA surface detector [56], also shown is the Auger spectrum [57] with a 10% energy scaling applied to make it agree with the TA SD flux.

7. Summary

The Telescope Array Low Energy extension was constructed to extend TA’s study of the spectrum and composition of cosmic rays down to the $10^{16.5} - 10^{18.5}$ eV regime. This is the energy range in which the transition from cosmic rays of galactic origin to those of extragalactic origin is thought to occur. Although several experiments have already seen hints of a “second knee” structure in the 10^{17} decade, they have different energy scales and flux normalizations, so that the actual energy of the feature was unknown. TALE overlaps with other TA spectra, so that TALE measurements will share a single energy scale with TA.

TALE consists of 10 high-elevation fluorescence telescopes and an in-fill array of 103 surface detectors. The TALE FD has been taking monocular data since 2013. We analyzed 1080 hours of TALE monocular FD data taken between June 2014 and March 2016. Events were reconstructed using a profile-constrained geometry fit that reconstructs the spatial trajectory and the longitudinal development of the extensive air shower in a single step. We demonstrated that this technique gives energy resolutions sufficient for spectrum measurement. In particular, we obtained a $\sim 15\%$ energy reconstruction resolution of Cherenkov-dominated showers pointing towards the detector. These events were previously rejected for spectrum measurements. Their inclusion allowed us to extend the lower threshold of TALE FD by more than another order of magnitude to $10^{15.3}$ eV.

Simulation based on CONEX, using the QGSJET-II.3 hadronic model are used to calculate the aperture and to study the detector resolutions. Monte Carlo vs. data comparisons showed good agreement in the distributions of impact parameter (R_p), zenith angle and azimuthal angle (ϕ). These quantities are directly tied to the aperture calculation. However, the shower maximum depth (X_{\max}) distribution in the MC, was adjusted to agree to the data. This last process removed any dependence on the composition assumption related to the dependence of X_{\max} to the underlying hadronic model.

We present the resulting spectrum spanning $10^{15.3} - 10^{18.3}$ eV. The systematic error on the flux is estimated to be about 30%, dominated by the overall uncertainty in energy scale of about 14%. The spectrum shown in Figure 20 shows a clear second knee near $10^{17.1}$ eV, along with an ankle-like structure at $10^{16.2}$ eV. At the lowest reach of our measurement, we also see the “first knee” at $\sim 10^{15.6}$ eV. The ratio of the energies of the two knees is tantalizingly close to the factor of 26 in the charge ratio of iron to protons. This suggests that the two “knee” structures represent the ends of the galactic iron (second knee) and proton/helium (first knee) fluxes.

Acknowledgements

The Telescope Array experiment is supported by the Japan Society for the Promotion of Science (JSPS) through Grants-in-Aid for Specially Promoted Research JP21000002, for Scientific Research (S) JP19104006, for Specially Promoted Research JP15H05693, for Scientific Research (S) JP15H05741 and for Young Scientists (A) JPH26707011; by the joint research program of the Institute for Cosmic Ray Research (ICRR), The University of Tokyo; by the U.S. National Science Foundation awards PHY-0601915, PHY-1404495, PHY-1404502, and PHY-1607727; by the National Research Foundation of Korea (2015R1A2A1A01006870, 2015R1A2A1A15055344, 2016R1A5A1013277, 2007-0093860, 2016R1A2B4014967); by the Russian Academy of Sciences, RFBR grant 16-02-00962a (INR), IISN project No. 4.4502.13, and Belgian Science Policy under IUAP VII/37 (ULB). The foundations of Dr. Ezekiel R. and Edna Wattis Dumke, Willard L. Eccles, and George S. and Dolores Doré Eccles all helped with generous donations. The State of Utah supported the project through its Economic Development Board, and the University of Utah through the Office of the Vice President for Research. The experimental site became available through the cooperation of the Utah School and Institutional Trust Lands Administration (SITLA), U.S. Bureau of Land Management (BLM), and the U.S. Air Force. We appreciate the assistance of the State of Utah and Fillmore offices of the BLM in crafting the Plan of Development for the site. Patrick Shea assisted the collaboration with valuable advice on a variety of topics. The people and the officials of Millard County, Utah have been a source of steadfast and warm support for our work which we greatly appreciate. We are indebted to the Millard County Road Department for their efforts to maintain and clear the roads which get us to our sites. We gratefully acknowledge the contribution from the technical staffs of our home institutions. An allocation of computer time from the Center for High Performance Computing at the University of Utah is gratefully acknowledged.

Appendix A

Spectrum data listed in table 6

Table 6: Spectrum data

energy-bin	Num. Events	$E^3 j(E) \pm \sigma_{stat.} \pm \sigma_{sys.}$
15.30-15.35	7207	$2.864 \pm 0.034 + 1.585 - 1.132$
15.35-15.40	10663	$2.965 \pm 0.029 + 1.073 - 1.056$
15.40-15.45	13829	$3.052 \pm 0.026 + 0.897 - 0.811$
15.45-15.50	17040	$3.187 \pm 0.024 + 0.705 - 0.724$
15.50-15.55	19821	$3.327 \pm 0.024 + 0.485 - 0.603$
15.55-15.60	21628	$3.398 \pm 0.023 + 0.341 - 0.432$
15.60-15.65	22664	$3.411 \pm 0.023 + 0.311 - 0.311$
15.65-15.70	22553	$3.352 \pm 0.022 + 0.463 - 0.463$
15.70-15.75	24448	$3.405 \pm 0.022 + 0.413 - 0.413$
15.75-15.80	24241	$3.393 \pm 0.022 + 0.200 - 0.277$
15.80-15.85	23375	$3.310 \pm 0.022 + 0.294 - 0.301$
15.85-15.90	22309	$3.288 \pm 0.022 + 0.329 - 0.400$
15.90-15.95	20576	$3.231 \pm 0.023 + 0.447 - 0.456$
15.95-16.00	18558	$3.161 \pm 0.023 + 0.519 - 0.454$
16.00-16.05	16685	$3.132 \pm 0.024 + 0.526 - 0.482$
16.05-16.10	14820	$3.079 \pm 0.025 + 0.561 - 0.471$
16.10-16.15	13181	$3.074 \pm 0.027 + 0.555 - 0.536$
16.15-16.20	11428	$3.030 \pm 0.028 + 0.640 - 0.558$
16.20-16.25	9788	$2.978 \pm 0.030 + 0.673 - 0.526$
16.25-16.30	8462	$2.992 \pm 0.033 + 0.642 - 0.513$
16.30-16.35	7363	$3.032 \pm 0.035 + 0.627 - 0.510$
16.35-16.40	6432	$3.074 \pm 0.038 + 0.621 - 0.536$
16.40-16.45	5576	$3.068 \pm 0.041 + 0.648 - 0.478$
16.45-16.50	4942	$3.150 \pm 0.045 + 0.582 - 0.620$
16.50-16.55	4168	$3.075 \pm 0.048 + 0.753 - 0.434$
16.55-16.60	3759	$3.149 \pm 0.051 + 0.517 - 0.733$
16.60-16.65	3028	$3.254 \pm 0.059 + 0.987 - 0.505$
16.65-16.70	2686	$3.275 \pm 0.063 + 0.602 - 0.565$
16.70-16.75	2334	$3.365 \pm 0.070 + 0.701 - 0.737$
16.75-16.80	1914	$3.262 \pm 0.075 + 0.915 - 0.568$
16.80-16.85	1660	$3.317 \pm 0.081 + 0.699 - 0.546$
16.85-16.90	1456	$3.395 \pm 0.089 + 0.669 - 0.737$
16.90-16.95	1197	$3.269 \pm 0.094 + 0.906 - 0.452$
16.95-17.00	1083	$3.495 \pm 0.106 + 0.561 - 0.686$
17.00-17.05	914	$3.409 \pm 0.113 + 0.832 - 0.482$
17.05-17.10	824	$3.504 \pm 0.122 + 0.577 - 0.511$
17.10-17.15	739	$3.491 \pm 0.128 + 0.596 - 0.445$
17.15-17.20	677	$3.422 \pm 0.132 + 0.500 - 0.683$
17.20-17.25	569	$2.952 \pm 0.124 + 0.736 - 0.264$
17.25-17.30	544	$2.901 \pm 0.124 + 0.285 - 0.240$
17.30-17.35	524	$2.916 \pm 0.127 + 0.263 - 0.263$
17.35-17.40	540	$3.128 \pm 0.135 + 0.381 - 0.381$
17.40-17.45	498	$3.055 \pm 0.137 + 0.423 - 0.438$
17.45-17.50	448	$2.921 \pm 0.138 + 0.488 - 0.437$
17.50-17.55	400	$2.755 \pm 0.138 + 0.485 - 0.236$
17.55-17.60	384	$2.828 \pm 0.144 + 0.265 - 0.387$
17.60-17.70	614	$2.530 \pm 0.103 + 0.865 - 0.752$
17.70-17.80	490	$2.548 \pm 0.115 + 0.611 - 0.518$
17.80-17.90	380	$2.498 \pm 0.128 + 0.449 - 0.586$
17.90-18.00	282	$2.440 \pm 0.146 + 0.710 - 0.659$
18.00-18.10	191	$2.308 \pm 0.167 + 0.824 - 0.646$
18.10-18.20	117	$1.996 \pm 0.185 + 0.794 - 0.309$
18.20-18.30	85	$2.071 \pm 0.225 + 0.832 - 1.067$

References

- [1] C. T. Hill and D. N. Schramm, *The Ultrahigh-Energy Cosmic Ray Spectrum*, *Phys. Rev. D* **31** (1985) 564.
- [2] V. S. Berezhinsky and S. I. Grigor'eva, *A Bump in the ultrahigh-energy cosmic ray spectrum*, *Astron. Astrophys.* **199** (1988) 1.
- [3] V. Berezhinsky, *Dip in uhecr and transition from galactic to extragalactic cosmic rays*, *astro-ph/0509069*.
- [4] R. U. Abbasi *et al.* [HiRes Collaboration], *A Study of the composition of ultrahigh energy cosmic rays using the High Resolution Fly's Eye*, *Astrophys. J.* **622**, 910 (2005)
- [5] R. U. Abbasi *et al.*, *Study of Ultra-High Energy Cosmic Ray composition using Telescope Arrays Middle Drum detector and surface array in hybrid mode*, *Astropart. Phys.* **64**, 49 (2015)
- [6] R. Aloisio, V. Berezhinsky and P. Blasi, *Ultra high energy cosmic rays: implications of Auger data for source spectra and chemical composition*, *JCAP* **1410**, no. 10, 020 (2014)
- [7] D. J. Bird *et al.* [HiRes Collaboration], *The Cosmic ray energy spectrum observed by the Fly's Eye*, *Astrophys. J.* **424**, 491 (1994).
- [8] Abu-Zayyad, T. *et al.* [HiRes-MIA Collaboration], *Measurement of the cosmic ray energy spectrum and composition from 10^{17} eV to $10^{18.3}$ eV using a hybrid fluorescence technique*, *Astrophys. J.* **557**, 686-699 (2001)
- [9] M. Nagano *et al.*, *Energy spectrum of primary cosmic rays above 10^{17} -eV determined from the extensive air shower experiment at Akeno*, *J. Phys. G* **18**, 423 (1992).
- [10] V. P. Egorova *et al.*, *The Spectrum features of UHECRs below and surrounding GZK*, *Nucl. Phys. Proc. Suppl.* **136**, 3 (2004)
- [11] T. Nonaka *et al.*, *The Surface Detector Array of the Telescope Array Experiment*, *Nucl.Instrum.Meth.* **A689**, 87-97 (2012)
- [12] Abu-Zayyad, T. and Aida, R. and Allen, M. and Anderson, R. and Azuma, R. *et al.*, *The Energy Spectrum of Telescope Array's Middle Drum Detector and the Direct Comparison to the High Resolution Fly's Eye Experiment*, *Astropart.Phys.* **39-40**, 109-119 (2012)
- [13] Tokuno, H. and Tameda, Y. and Takeda, M. and Kadota, K. and Ikeda, D. *et al.*, *New air fluorescence detectors employed in the Telescope Array experiment*, *Nucl.Instrum.Meth.* **A676**, 54-65 (2012)
- [14] Teshima, M. and Ohoka, H. and Matsubara, Y. and Hara, T. and Hatano, Y. *et al.*, *Expanded Array for Giant Air Shower Observation at Akeno*, *Nucl.Instrum.Meth.* **A247**, 399 (1986)
- [15] Sokolsky, P., *Final Results from the High Resolution Fly's Eye (HiRes) Experiment*, *Nucl.Phys.Proc.Suppl.* **212-213**, 74-78 (2011)
- [16] T. Abu-Zayyad *et al.* [Telescope Array Collaboration], *The Cosmic Ray Energy Spectrum Observed with the Surface Detector of the Telescope Array Experiment*, *Astrophys. J.* **768** (2013) L1
- [17] R. U. Abbasi *et al.* [Telescope Array Collaboration], *Indications of Intermediate-Scale Anisotropy of Cosmic Rays with Energy Greater Than 57 EeV in the Northern Sky Measured with the Surface Detector of the Telescope Array Experiment*, *Astrophys. J.* **790**, L21 (2014)
- [18] G.B. Thomson *et al.*, *The Telescope Array Low Energy Extension (TALE)*, in proceedings of *International Cosmic Ray Conference* **3**, 337-339 (2011)
- [19] Boyer, J. H. and Knapp, B. C. and Mannel, E. J. and Seman, M., *FADC-based DAQ for HiRes Fly's Eye*, *Nucl.Instrum.Meth.* **A482**, 457-474 (2002)

- [20] Zundel, Z. J., *Spectrum Measurement with the Telescope Array Low Energy Extension (TALE) Fluorescence Detector*, *Ph.D. Thesis, University of Utah*, (2016), Chapter 4.
- [21] J. D. Smith *et al.*, *Absolute GPS time event generation and capture for remote locations*, in proceedings of *International Cosmic Ray Conference*, 825-827 (2001)
- [22] D. Bergman, Y. Tsunesada, J.F. Krizmanic, Y. Omura *jNICHE: Prototype detectors of a non-imaging Cherenkov array at the TA site*, *PoS ICRC 2017*, 415 (2017) in proceedings of *International Cosmic Ray Conference*, 825-827 (2001)
- [23] Abu-Zayyad, T. *et al.* [Telescope Array Collaboration], *Cosmic Rays Energy Spectrum observed by the TALE detector using Cerenkov light*, *PoS ICRC 2015*, 422 (2016)
- [24] R. M. Baltrusaitis *et al.*, *The Utah Fly's Eye Detector*, *Nucl. Instrum. Meth. A* **240**, 410 (1985)
- [25] AbuZayyad, T. *The Energy Spectrum of Ultra High Energy Cosmic Rays*, PhD thesis, University of Utah (2000)
- [26] Abbasi, R.U. *et al.*, *First Observation of the Greisen-Zatsepin-Kuzmin suppression*, *Phys.Rev.Lett.* **100**, 101101 (2008)
- [27] Bergmann, T. *et al.*, *One-dimensional Hybrid Approach to Extensive Air Shower Simulation*, *Astropart.Phys.* **26**, 420-432 (2007)
- [28] Heck, D. *et al.*, *CORSIKA: A Monte Carlo code to simulate extensive air showers*, *FZKA-6019* (1998)
- [29] Bernlohr, Konrad, *Simulation of Imaging Atmospheric Cherenkov Telescopes with CORSIKA and sim.telarray*, *Astropart.Phys.* **30**, 149-158 (2008)
- [30] Lafebre, S. *et al.*, *Universality of electron-positron distributions in extensive air showers*, *Astropart.Phys.* **31** 243-254 (2009)
- [31] Greisen, K., , *Prog. Cosm. Ray Phys.* **3** 1 (1956)
- [32] Kamata, K., and Nishimura, J., , *Prog. Theor. Phys. Suppl.* **6** 93 (1958)
- [33] F. Kakimoto, E. C. Loh, M. Nagano, H. Okuno, M. Teshima and S. Ueno, *A Measurement of the air fluorescence yield*, *Nucl. Instrum. Meth. A* **372**, 527 (1996).
- [34] J. W. Belz *et al.* [FLASH Collaboration], *Measurement of pressure dependent fluorescence yield of air: Calibration factor for UHECR detectors*, *Astropart. Phys.* **25**, 129 (2006)
- [35] F. Nerling, J. Bluemer, R. Engel and M. Risse, *Universality of electron distributions in high-energy air showers: Description of Cherenkov light production*, *Astropart. Phys.* **24**, 421 (2006)
- [36] <http://ready.arl.noaa.gov/gdas1.php>
- [37] Gaisser, T.K., *Spectrum of cosmic-ray nucleons, kaon production, and the atmospheric muon charge ratio*, *Astropart.Phys.* **35** 801-806 (2012)
- [38] <https://root.cern/doc/master/classTFractionFitter.html>
- [39] R. J. Barlow and C. Beeston, *Fitting using finite Monte Carlo samples*, *Comput. Phys. Commun.* **77**, 219 (1993).
- [40] Toshihiro Fujii *et al.* *A systematic uncertainty on the energy scale of the Telescope Array fluorescence detectors*, *PoS ICRC 2017*, 524 (2017).
- [41] R. U. Abbasi *et al.* [HiRes Collaboration], *Measurement of the flux of ultrahigh energy cosmic rays from monocular observations by the High Resolution Fly's Eye experiment*, *Phys. Rev. Lett.* **92**, 151101 (2004)

- [42] R. U. Abbasi *et al.* [HiRes Collaboration], *Measurement of the Flux of Ultra High Energy Cosmic Rays by the Stereo Technique*, *Astropart. Phys.* **32**, 53 (2009)
- [43] T. Tomida *et al.*, *The atmospheric transparency measured with a LIDAR system at the Telescope Array experiment*, *Nucl. Instrum. Meth. A* **654**, 653 (2011) doi:10.1016/j.nima.2011.07.012 [arXiv:1109.1196 [astro-ph.IM]].
- [44] J. Rosado, F. Blanco and F. Arqueros, *Comparison of available measurements of the absolute air-fluorescence yield and determination of its global average value*, *AIP Conf. Proc.* **1367**, 34 (2011) doi:10.1063/1.3628711 [arXiv:1104.0894 [astro-ph.IM]].
- [45] R. Cady, *A world average of fluorescence yield measurements*, *AIP Conf. Proc.* **1367**, 40 (2011).
- [46] R. U. Abbasi *et al.*, *The hybrid energy spectrum of Telescope Arrays Middle Drum Detector and surface array*, *Astropart. Phys.* **68**, 27 (2015).
- [47] B. Peters, *Primary cosmic radiation and extensive air showers*, *Il Nuovo Cimento* **22** 800-819 (1961)
- [48] N. M. Budnev *et al.*, *The Cosmic Ray Mass Composition in the Energy Range 10^{15} - 10^{18} eV measured with the Tunka Array: Results and Perspectives*, *Nucl. Phys. Proc. Suppl.* **190** (2009) 247
- [49] W. D. Apel *et al.*, *KASCADE-Grande measurements of energy spectra for elemental groups of cosmic rays*, *Astropart. Phys.* **47**, 54 (2013)
- [50] S. P. Knurenko *et al.*, *Cosmic ray spectrum in the energy range $1.0E15$ - $1.0E18$ eV and the second knee according to the small Cherenkov setup at the Yakutsk EAS array*, *arXiv:1310.1978 [astro-ph.HE]*.
- [51] N. Budnev *et al.*, *Tunka-25 Air Shower Cherenkov array: The main results*, *Astropart. Phys.* **50-52**, 18 (2013).
- [52] V. V. Prosin *et al.*, *Tunka-133: Results of 3 year operation*, *Nucl. Instrum. Meth. A* **756**, 94 (2014).
- [53] W. D. Apel *et al.*, *The spectrum of high-energy cosmic rays measured with KASCADE-Grande*, *Astropart. Phys.* **36** (2012) 183.
- [54] K. Rawlins [IceCube Collaboration], *Cosmic ray spectrum and composition from three years of IceTop and IceCube*, *J. Phys. Conf. Ser.* **718**, no. 5, 052033 (2016).
- [55] R. U. Abbasi *et al.* [Telescope Array Collaboration], *The energy spectrum of cosmic rays above $10^{17.2}$ eV measured by the fluorescence detectors of the Telescope Array experiment in seven years*, *Astropart. Phys.* **80**, 131 (2016)
- [56] C. Jui, *Summary of Results from the telescope Array Experiment*, *PoS ICRC* **2015**, 035 (2016).
- [57] A. Schulz [Pierre Auger Collaboration], *The measurement of the energy spectrum of cosmic rays above $3x10^{17}$ eV with the Pierre Auger Observatory*, *PoS ICRC* **2013**, 0769 (2013).